# Non-monotonic effects of persistent time and amplitude in fluctuating tension on the dynamics of the two-dimensional confluent tissue

Takaki Yamamoto, <sup>1, 2, \*</sup> Daniel M. Sussman, <sup>3</sup> Tatsuo Shibata, <sup>2</sup> and M. Lisa Manning <sup>4, 5, †</sup>

<sup>1</sup> Nonequilibrium Physics of Living Matter RIKEN Hakubi Research Team,

RIKEN Center for Biosystems Dynamics Research,

<sup>2-2-3</sup> Minatojima-minamimachi, Chuo-ku, Kobe 650-0047, Japan

<sup>2</sup> Laboratory for Physical Biology, RIKEN Center for Biosystems Dynamics Research, Kobe 650-0047, Japan

<sup>3</sup> Department of Physics, Emory University, Atlanta, GA, USA

<sup>4</sup> Department of Physics, Syracuse University, Syracuse, New York 13244, USA

<sup>5</sup> BioInspired Institute, Syracuse University, Syracuse, New York 13244, USA

(Dated: August 20, 2020)

In development and homeostasis, multi-cellular systems exhibit spatial and temporal heterogeneity in their biochemical and mechanical properties. Nevertheless, it remains unclear how spatiotemporally heterogeneous forces affect the dynamical and mechanical properties of confluent tissue. To address this question, we study the dynamical behavior of the two-dimensional cellular vertex model for epithelial monolayers in the presence of fluctuating cell-cell interfacial tensions, which is a biologically relevant source of mechanical spatiotemporal heterogeneity. In particular, we investigate the effects of the amplitude and persistence time of fluctuating tension on the tissue dynamics. We unexpectedly find that the long-time diffusion constant describing cell rearrangements depends non-monotonically on the persistence time, while it increases monotonically as the amplitude increases. Our analysis indicates that the non-monotonicity appears due to a competition between two opposite effects: increasing amplitude and persistence time induces higher-order vertices, *i.e.* rosette structure, which constrains the motion of edges and slows tissue dynamics, while larger amplitude and persistence time promote the cell rearrangement by driving larger motion of vertices.

### I. INTRODUCTION

Spatiotemporal heterogeneity plays important roles in various biological processes [1–12]. At the molecular scale, molecular motors such as kinesin [1–3], myosin [4] and F1-ATPase [3, 5] utilize thermal temporal fluctuations to function. At scale of single cells, structures such as the cytoskeleton and focal adhesions spatially selforganize to execute necessary cellular functions [6, 7]. Finally, at the multi-cellular scale, spatiotemporal heterogeneity of gene expression and downstream cell differentiation are necessary for tissue homeostasis [8] and proper development [9]. Cooperatively with this biochemical heterogeneity, multi-cellular systems control mechanical properties and cell motility to establish and maintain structures such as compartments and organs, and drive morphogenetic processes such as gastrulation and invagination [10-12]. Therefore, it is essential to understand how spatiotemporally heterogeneous forces in multi-cellular systems affect the dynamical and mechanical properties of the tissue.

Work over the past decade has suggested that the physics of jamming and glasses is a good starting point for understanding the mechanics and dynamics of multicellular tissues. Experiments have shown that dense biological tissues undergo solid-to-fluid transitions [13–17], and near such transitions many systems, including Madin-Darby canine kidney (MDCK) cells [16] and

primary human bronchial epithelial cells (HBECs) [13] exhibit heterogeneous dynamics that are a hallmark of glassy dynamics. Recent work in vivo suggests that zebrafish use a spatial gradient in the fluid-to-solid transition to help drive body axis elongation [15]. Also, theoretical studies have elucidated such glassy behaviors using mathematical models of confluent tissues such as the cellular vertex model (CVM) [18–20], the voronoi model (VM) [18, 21] and the cellular Potts models [22]. For instance, a VM study by Bi et al. reported that fluctuations induced by self-propulsion of the cells works in concert with cell mechanics to induce solid-to-fluid transitions [21]. Sussman et al. demonstrated anomalous glassy behavior in 2D confluent tissue driven by Brownian fluctuations in both CVM and VM [18]. Very recent work, initiated independently and concurrently with the work reported here, studied the effect of fluctuating tensions on confluent [19] and non-confluent [20] CVM models. In general, all of these models agree that increasing either the magnitude of the fluctuating forces, or the persistence of such forces, can drive systems from the solid phase to the fluid phase.

In contrast, Yan et al. report on a mechanism that can drive a confluent tissue in the other direction, from a fluid state to a solid state. While all VM and most CVM models restrict allowable topologies to 3-fold coordinated vertices, Yan and collaborators demonstrate that introducing rosette structures, which are n-fold vertices (n > 3), imposes topological constraints on the network of the CVM that can rigidify the tissue [23] in static calculations. Since rosette structures appear frequently during developmental processes [24–26], it is likely that rigid-

<sup>\*</sup> takaki.yamamoto@riken.jp

<sup>†</sup> memanning@gmail.com

ification driven by multi-fold vertex formation is competing with fluctuation-driven fluidization. It is an open question how these two processes interact with each other to generate tissue dynamics and remodeling. Interesting recent work has studied the effect of explicit pinning of rosette structures in a fluctuating system, though pinning timescales are put in by hand [27].

One obvious framework that could naturally give rise to both fluctuations and rosette formation is spatiotemporally fluctuating tension along cell-cell interfaces. Such fluctuations are regularly observed in experiments [28] and controlled by expression and localization of cytoskeletal and adhesion molecules. For example, fluctuating tension was previously reported for the dynamics of *Drosophila* pupal notum, which is a 2D confluent epithelial tissue [28]. In [28], the authors showed that a 2D CVM with fluctuating tension with some amplitude and persistent time is consistent with the experimental observations. A study concurrent and independent of the work we report here, by Kranjc [19], analyzed the phase space of fluid-solid transitions in similar CVM models with fluctuating tension. However, it appears that the parameter range of tensions and persistence times studied in that work focuses on the regime where fluidization always dominates over rosette formation. Given experimental observations, this may not be the full experimentally relevant range. In this work, we extend those previous ideas to characterize how fluctuating tensions across a broad parameter range affect the global tissue mechanics and local cell motion in 2D confluent tissues. We find strongly non-monotonic mechanical response and cell diffusion as a function of the magnitude of the stress fluctuations and their persistence time, consistent with the picture that fluidization due to fluctuations competes with rigidification due to rosette formation.

#### II. RESULTS

We model the dynamics of a 2D confluent tissue using the well-studied 2D cellular vertex model (CVM), where the cells are represented by polygons, and the cellular deformation and motion are described by the displacement of the vertices and change in the network topology [29]. In the 2D CVM, the cellular mechanics and dynamics are governed by the mechanical energy. The non-dimensionalized mechanical energy  $\epsilon$  of the epithelial tissue is written as a functional of the vertex coordinates  $\{\vec{r}_i\}$ ;

$$\epsilon(\{\vec{r}_i\}) = \frac{1}{2} \sum_{\alpha=1}^{N} \left\{ k_{\alpha} (a_{\alpha} - a_{0,\alpha})^2 + (p_{\alpha} - p_{0,\alpha})^2 \right\} + \sum_{(i,j)} \Delta \lambda_{ij}(t) \ell_{ij}, \tag{1}$$

where  $\alpha$  and N denote the label of each cell and the total number of the cells.  $a_{\alpha}$  and  $p_{\alpha}$  are the area and perimeter of cell  $\alpha$ .  $a_{0,\alpha}$  and  $p_{0,\alpha}$  are the preferred area and

perimeter, respectively. We choose the length scale to satisfy the average cell area  $\langle a_{\alpha} \rangle = 1$ .  $k_{\alpha}$  is the relative area stiffness with respect to the perimeter stiffness of the cell. Furthermore, we introduce the time-dependent fluctuating part of the tension  $\Delta \lambda_{ij}(t)$  as the last term in Eq. (1), where  $\ell_{ij}$  is the edge length between the *i*th and *j*th vertices and the summation runs over the pairs (i,j) of the vertices composing the edges. Based on this mechanical energy, the dynamics of the vertices is described by the following time-evolution equation;

$$\eta \frac{d\vec{r}_i}{dt} = -\frac{\partial \epsilon(\{\vec{r}_i\})}{\partial \vec{r}_i},\tag{2}$$

where  $\eta$  is the friction coefficient.

We introduce the dynamics of fluctuating part of tension  $\Delta \lambda_{ij}(t)$  as a general form using a colored Gaussian noise by Ornstein-Uhlenbeck process as follows [19, 28];

$$\frac{d\Delta\lambda_{ij}(t)}{dt} = -\frac{\Delta\lambda_{ij}(t)}{\tau} + \xi_{ij}(t), \tag{3}$$

where  $\xi_{ij}(t)$  is a white Gaussian noise satisfying  $\langle \xi_{ij}(t) \rangle = 0$  and  $\langle \xi_{ij}(t_1) \xi_{kl}(t_2) \rangle = 2\sigma^2/\tau \delta_{ik} \delta_{jl} \delta(t_1 - t_2)$ . Here,  $\Delta \lambda_{ij}(t)$  satisfies  $\langle \Delta \lambda_{ij}(t) \rangle = 0$  and  $\langle \Delta \lambda_{ij}(t_1) \Delta \lambda_{kl}(t_2) \rangle = \delta_{ik} \delta_{jl} \sigma^2 e^{-|t_1 - t_2|/\tau}$ . The characteristic time scale of the fluctuating tension is determined by the persistence time  $\tau$ .

In this study, we investigate the effect of the amplitude  $\sigma$  and persistent time  $\tau$  of the fluctuating tension on the cellular dynamics. In our numerical simulation, we solve Eq. (2) using forward Euler method with a time step dt = 0.01. We initially prepare hexagonally-patterned 340 cells in a squared area with periodic boundary condition, then run the simulation with a large amplitude of fluctuation in tension to randomize the cellular configuration for 100 natural time units ( $\sigma = 0.35, \tau = 1$ ). After the randomization, we simulate dynamics in the system with the target values of  $\sigma$  and  $\tau$  for  $10^4$  natural time units to initialize the system, then report dynamical data over an additional  $10^5$  natural time units. As is standard, we perform T1 transitions by flipping edges with a length below a threshold  $l_{\rm th}$  in clockwise direction by 90°, if the energy decreases after the T1 transition. We set  $l_{\rm th}$  to 5% of the length of an edge of a regular hexagonal cell with area 1.

Unfortunately, there is little experimental data describing how tensions evolve after a T1 transition. In the absence of such data, one could envision several scenarios for how to specify the tension on the newly formed edge. We consider three options in this manuscript, illustrated schematically in Fig. 1. In the first "persistent model", we keep the same value of the tension  $\Delta \lambda_{ij}(t)$  after the T1 transition as was on the shrinking edge before the T1 transition. In the second "resetting model",  $\Delta \lambda_{ij}(t)$  along the new edge is set to zero after the T1 transitions. In the last "resampling model", we resample  $\Delta \lambda_{ij}(t)$  from the normal distribution  $N(0, \sigma^2)$  with zero mean and variance  $\sigma^2$ , which is the stationary distribution of Ornestein-Uhlenbeck process described by Eq. (3).

In the first part of this manuscript, we focus on data from the persistent model, and report on similarities and differences between these scenarios in the last section.

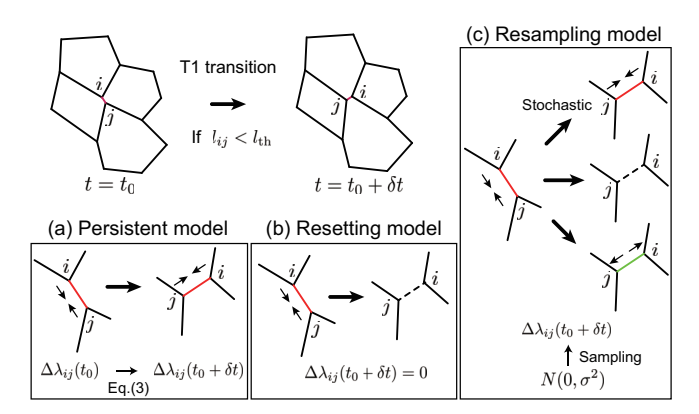


FIG. 1. Schematic illustration of three vertex models with different ways of updating  $\Delta \lambda_{ij}$  upon a T1 transition: (a) the persistent model, (b) the resetting model and (c) the resampling model. The illustration shows how  $\Delta \lambda_{ij}$  is renewed upon each T1 transition. In the box for each model, the red solid, the black dashed and the green solid edges show the edges with positive, zero-valued and negative  $\Delta \lambda_{ij}$ , respectively. The only edges with positive  $\Delta \lambda_{ij}$  before a T1 transition are shown, because such edges should tend to shrink more frequently than those with negative  $\Delta \lambda_{ij}$ .

First, we study the qualitative effect of varying the overall magnitude  $\sigma$  and persistence  $\tau$  of stress fluctuations on cellular structure. Snapshots of the cellular configuration from the numerical simulations for different sets of  $\sigma$  and  $\tau$  for fixed  $p_0 = 3.9$  are shown in Fig. 2. For fixed  $\sigma = 0.3$  (Fig. 2(a-c)), we found that the cellular shape is more irregular for larger  $\tau$ , while larger  $\sigma$  gives more irregular cell shapes for fixed  $\tau = 1$  (Fig. 2(b) and (d)).

Fig. 2(e) quantifies the cell shape index  $q_{\alpha} = p_{\alpha}/\sqrt{a_{\alpha}}$ , which tends to increase when the cellular shape is anisotropic or the number of edges composing the cell is large. This panel confirms that cell shape index increase with increasing  $\tau$  and  $\sigma$ . This not surprising, as increasing  $\tau$  and  $\sigma$  increases the number of persistently shrinking (large positive  $\Delta \lambda_{ij}$ ) and expanding (large negative  $\Delta \lambda_{ij}$ ) edges.

There is one surprise. Although previous work in vertex models has identified a strong correlation between cell shape and tissue fluidity, it is clear from the insets of Fig. 2(a-c) illustrating cell trajectories that there is a nonmonotonic behavior for cell diffusivity as a function of increasing  $\tau$ , despite the fact that cell shapes become more irregular with increasing  $\tau$ . Similarly, Fig. 2(e) illustrates that there is a small- $\tau$  regime where the cell shape depends sensitively on  $\tau$ , and a large  $\tau$  regime where cell shape becomes almost independent of  $\tau$ . Moreover, at these larger values of  $\tau$ , irregular cell shapes coexist with many very short edges, highlighted with square symbols

Fig. 2, a point we will return to later.

To quantitatively characterize the cellular dynamics and begin to understand the origin of the observed nonmonotonic behavior, we calculate the mean-squared displacement (MSD) of the area centroid of the cells. Example cell trajectories are shown in Fig. 2. In Fig. 3(a), we show the MSD curves as a function of the time t for  $\tau = 1$  and  $p_0 = 3.9$ . The curves exhibit ballistic behavior with MSD  $\sim t^2$  at short time scales  $t \ll \tau$ . At long time scales  $\tau \ll t$ , the cellular dynamics exhibit diffusive behavior with MSD  $\sim$  t. Notably, we found that the MSD exhibits a sub-diffusive plateau characterized by MSD  $\sim$  t<sup> $\alpha$ </sup> with 0 <  $\alpha$  < 1 at intermediate time scales. This plateau, also seen in CVM simulations with Brownian noise on the vertices [18], is a characteristic feature of glasses and indicates that cells are being caged by the neighbors at intermediate timescales. The plateau becomes less prominent at large values of  $\sigma$ , suggesting that  $\sigma$  is playing a role similar to an effective temperature, where the system becomes more fluid-like as  $\sigma$  increases the overall level of fluctuations. We further characterize the dynamics by estimating the diffusion constant  $D = \lim_{t\to\infty} MSD(t)/4t$  for values of  $t > 10^4$  for different  $\tau$  and  $\sigma$  as shown in Fig. 3(b). The diffusion constant D exhibits non-monotonic dependence on  $\tau$ , where D is maximized at intermediate  $\tau \sim 1-10$ . This quantitatively confirms the cellular dynamics exhibits two different regimes at small and large  $\tau$ , respectively, which we discuss in detail below.

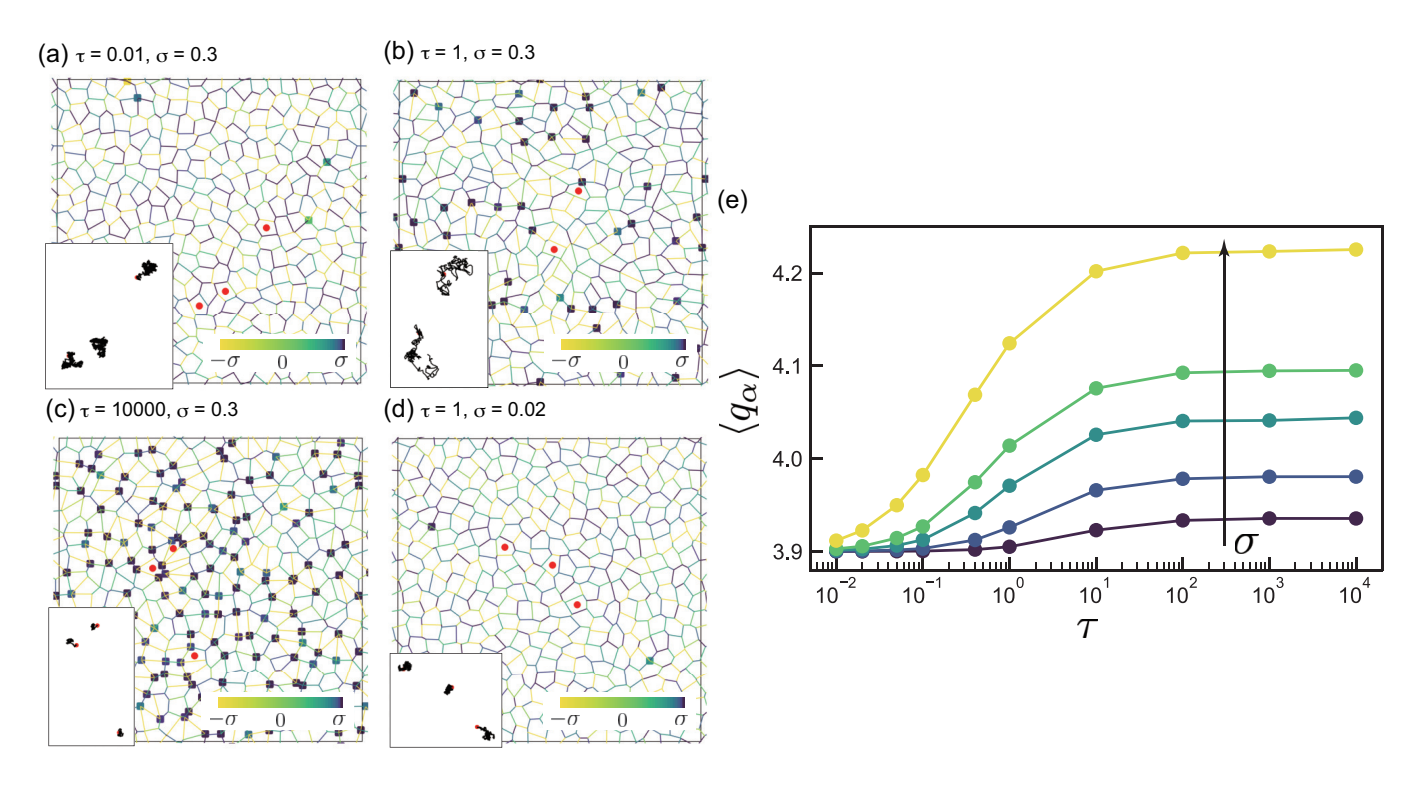
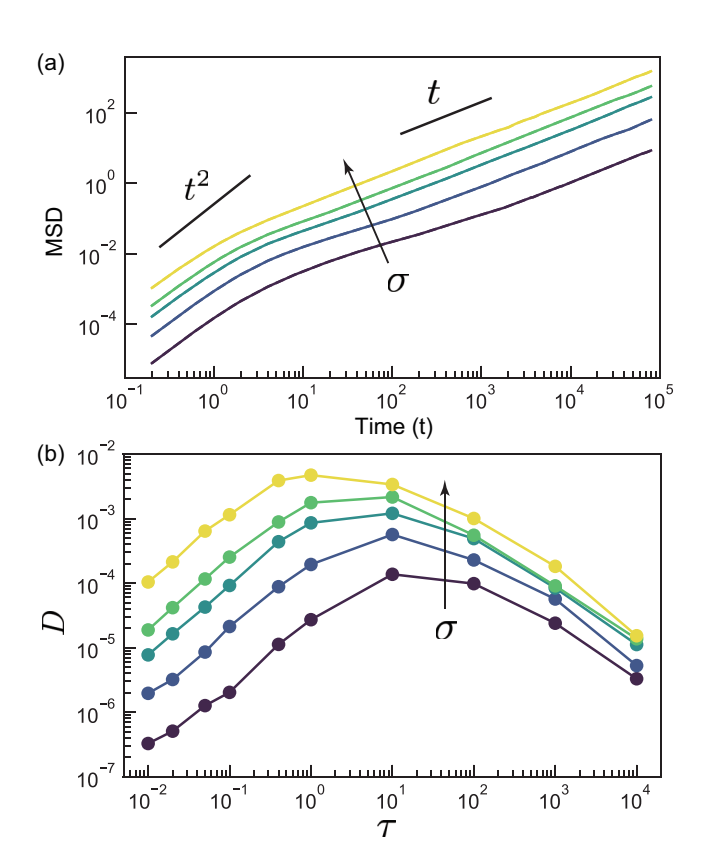


FIG. 2. Snapshots of the cellular configurations obtained in our numerical simulation with different  $\tau$  and  $\sigma$ : (a)  $\tau = 0.01, \sigma = 0.3$ , (b)  $\tau = 1, \sigma = 0.3$ , (c)  $\tau = 10000, \sigma = 0.3$ , (d)  $\tau = 1, \sigma = 0.02$ . We draw the edges with the color mapping the value of  $\Delta \lambda_{ij}$ . The color is mapped to  $\Delta \lambda_{ij}$  ranging in  $[-\sigma, \sigma]$  using the color map in each figure. If  $\Delta \lambda_{ij} < -\sigma \ (\Delta \lambda_{ij} > \sigma)$ , we color the edge with the color corresponding to  $\Delta \lambda_{ij} = -\sigma \ (\Delta \lambda_{ij} = \sigma)$ . The trajectories of cells marked with red circles are also shown with black solid lines in the insets. We show the trajectories in the interval of 3000 time unit for (a)(c)(d) and 300 time unit for (b). In (b)(c)(d), we also highlight the trapped edges defined in the main text with the squares colored using the same color map as the other edges. (e) Average cell shape  $\langle q_{\alpha} \rangle$  for  $p_0 = 3.90$ .  $\sigma \in [0.02, 0.05, 0.10, 0.15, 0.30]$  (from dark color to light color).



We also investigate the effect of shape index  $p_0$ , another parameter which is known to control the rigidity of the tissue [13, 21, 30]. Previous 2D CVM studies showed that the confluent tissue becomes solid-like (fluid-like) for small (large)  $p_0$  with the transition point  $p_0^* \sim 3.81$  [13, 21]. In Fig. 4(a), we show the MSD curves for different  $p_0$  with fixed  $\tau = 10$  and  $\sigma = 0.05$ . For small  $p_0$ , the MSD curves show ballistic behaviors at short time scales, plateaus at intermediate time scales and diffusive behaviors at long time scales, indicating fluidity at the longest timescales. Again, the plateau indicating glassy dynamics is less prominent for large  $p_0$ , confirming that the tissue becomes less glassy and more fluid-like as  $p_0$ increases. Fig. 4 also show the MSD curves for different  $\sigma$  with fixed  $p_0 = 3.45$  and  $\tau = 10$ . Since  $p_0 = 3.45$  is well below  $p_0^*$ , for small  $\sigma$  the tissue is solid-like, exhibiting non-diffusive behavior at long timescales, but increasing  $\sigma$  leads to diffusion at long timescales, indicating fluidization of the tissue.

Therefore, in our model, the trio of parameters  $[p_0, \sigma, \tau]$  control the fluid-to-solid transition. In Fig. 4(c-e), we show the cross-sections of the three dimensional (3D) phase diagram of solid-to-fluid transition with respect to these parameters, where for simplicity we define the fluid-

FIG. 3. Cell dynamics as a function of the magnitude of stress fluctuations  $\sigma$  and the persistence of stress fluctuations  $\tau$ . (a) Mean-squared displacement (MSD) as a

solid transition by a threshold in the magnitude of the diffusion constant  $D^* = 10^{-4}$ . As highlighted in Fig. 4 (d) and (e), there is always a re-entrant fluid-solid transition as a function of  $\tau$ . To investigate the mechanisms driving this re-entrant behavior, we hereafter focus only on the case with  $p_0 = 3.9$ , since the re-entrant behavior is observed for many  $p_0$  values.

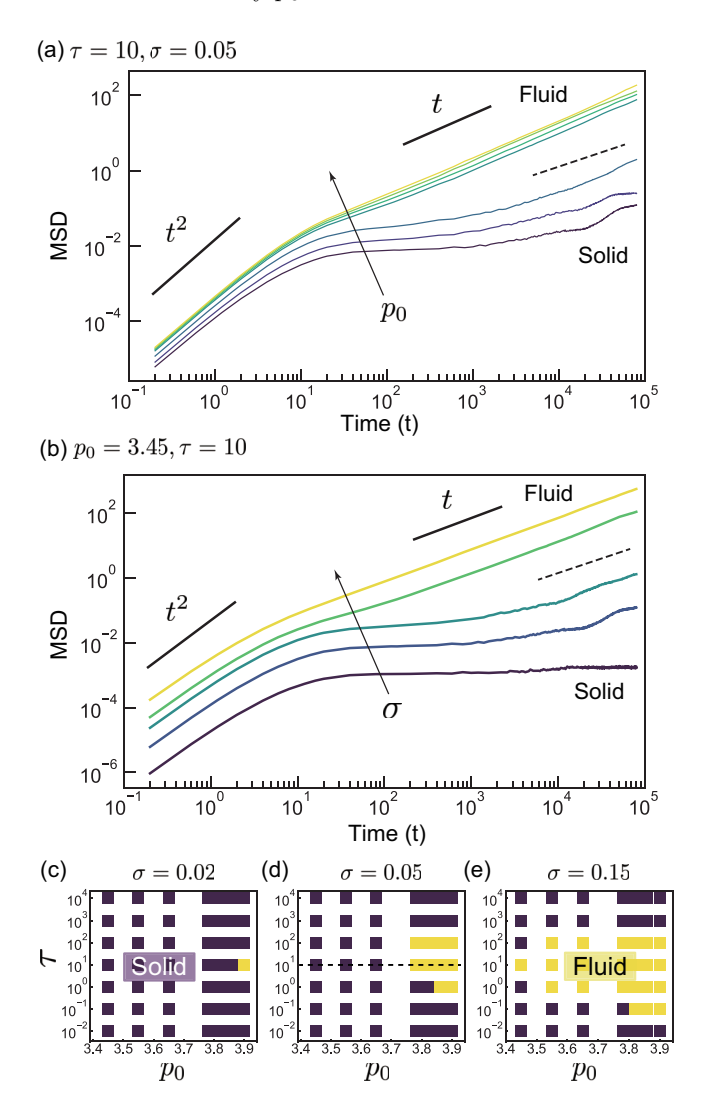


FIG. 4. Glassy behaviors of the confluent tissues for different  $p_0$ ,  $\tau$  and  $\sigma$ . (a)(b) The MSD curves for fixed  $(\tau = 10, \sigma = 0.05)$  and  $(p_0 = 3.45, \tau = 10)$  are shown. The dashed lines distinguish between the fluid-like and the solid-like phases. The solid lines are guides for eyes indicating the power law t and  $t^2$ , respectively. In (a),  $p_0 \in [3.45, 3.55, 3.65, 3.78, 3.82, 3.86, 3.90]$  (from dark color to light color). In (b),  $\sigma \in [0.02, 0.05, 0.10, 0.15, 0.30]$  (from dark color to light color). (c-e) Phase diagrams for the glassy behaviors. The solid-like  $(D < D^*)$  and fluid-like  $(D > D^*)$  tissues are shown as purple and yellow data points, respectively. The dashed line in (d) is the scanning line for the data in (a).

We first focus on the small- $\tau$  regime, where increasing  $\tau$  increases diffusion. Since cell diffusion is driven by

cell rearrangements that occur when a T1 edge shrinks to zero, we first think to investigate the characteristic timescale required for an edge of length l to shrink to zero. This is not a straightforward first-passage-time problem, however, as the edges in the tessellation cannot grow towards positive infinity. When the length rises significantly above unity, a T1 transition in a neighboring edge is likely to be triggered, generating a complicated absorbing boundary condition.

In addition, we are interested in the diffusion of a cell's center of mass. We anticipate that when an edge shrinks to zero and experiences a T1 transition, the cell center displaces a characteristic fraction of the distance over which the edge shrunk. Then a different edge shrinks and dominates the cell-center displacement. After many T1s, one arrives at a picture where the cell center of mass displaces as a memory-less chain of edge-shrinking events. Therefore, rather than focusing on the first-passage time statistics, we study the mean-field behavior of an edge length, and calculate the characteristic timescale over which it diffuses  $\tau_l$  in the absence of any boundary conditions. Assuming that the tension of the edge is determined only by the fluctuating part of the tension  $\Delta \lambda$ , we obtain the following time-evolution equation for the edge length l;

$$\frac{dl}{dt} = \Delta\lambda,\tag{4}$$

where the time-evolution of  $\Delta\lambda$  is given by Eq. (3) with  $l_{ij} = l$  and  $\Delta\lambda_{ij} = \Delta\lambda$ . Then the time evolution of the MSD of l is:  $\mathrm{MSD}_l(t) = 2\sigma^2\tau t + 2\sigma^2(\exp(-t/\tau) - 1)$  [31]. Accordingly, when  $t \gg \tau$ , the MSD of l scales as  $\mathrm{MSD}_l(t) = 2D_l t$ , where  $D_l = \sigma^2\tau$  is the diffusion constant of the edge length l. If we assume that this is the primary timescale driving cell rearrangements as discussed above, then we predict the total diffusion rate is simply  $D \sim D_l = \sigma^2\tau$ . This is in good agreement with numerical data for the small- $\tau$  regime as shown in Fig. 5. This confirms that in this regime, the fluidization generated by increasing  $\tau$  occurs because edges shrink more persistently.

This argument obviously breaks down in the large- $\tau$  regimes ( $\tau >\sim 1$ ), where the diffusion constant decreases with increasing  $\tau$ . An obvious way the argument could break down is that cells no longer rearrange when edges shrink to zero length, resulting in "trapped" edges. To test and quantify this idea, we focus on higher-order vertices, which are vertices where more than three cells meet, i.e. rosette structures. A CVM study by Yan et al. in the limit of zero fluctuations recently showed that rosette structures rigidify the epithelial tissue [23]. We thus hypothesize that the rigidification of the tissue driven by the rosette structures slows down the dynamics in our model in the large- $\tau$  regime.

However, unlike Ref [23], by construction our model only contains 3-fold coordinated vertices. Nevertheless, we hypothesize that in a dynamic simulation with finite fluctuations, vertices connected by very short interfaces

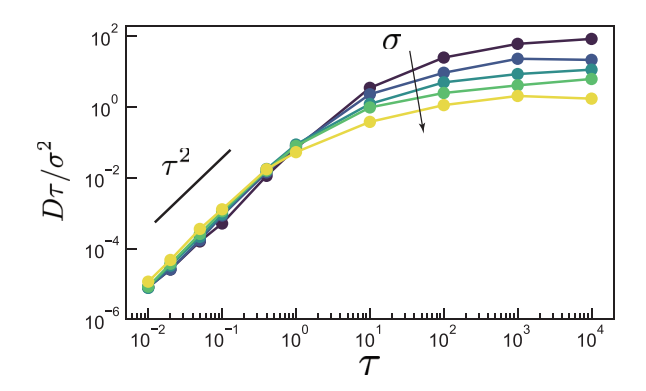


FIG. 5. Data collapse of the  $D\tau/\sigma^2$  vs.  $\tau$  plot to obtain the scaling relation  $D \propto \sigma^2 \tau$  in the small  $\tau$  regime. The solid line is a guide for eyes indicating the power law  $\tau^2$ .  $\sigma \in [0.02, 0.05, 0.10, 0.15, 0.30]$  (from dark color to light color).

restrict the dynamics in a manner similar to multi-fold coordinated vertices. Although higher-fold vertices are generically unstable in the fluid phase in CVMs with spatially homogeneous parameters [32], some of us previous reported similar behavior in a 2D CVM with extra interfacial tensions between two cell types, where nearly-4-fold vertices (with very short edges) are stabilized at the heterotypic interface [33]. Therefore it is not surprising that fluctuating heterotypic tensions could drive similar phenomena.

This is also consistent with our previous qualitative analysis of cellular structures: Fig. 2 (b, c) shows that an increasing number of very short edges, highlighted by square symbols, is associated with rigidification in the large- $\tau$  regime.

To better understand how short edges affect the dynamics in this model, we study their dynamics. Specifically, we track edges, indexed by i, that reach the threshold  $l_{\rm th}=0.03$  for checking a T1 transition. At every subsequent timestep where the system continuously remains below  $l_{\rm th}$ , we record the edge length  $l^i(t_T)$ , where  $t_T$  is the time since the edge first crossed  $l_{\rm th}$ .

To quantify this behavior, we study histograms of the edge lengths  $f(l^i)$  for various values of the trapping time  $t_T$ . (See Supplemental Fig. 8). For all but the longest timescales, there is a peak around  $l \sim 0.005$ , which is much smaller than the imposed T1 threshold  $l_{\rm th}$ , suggesting there is a population of edges where the dynamics drives them to remain very short. Such edges must remain short either because accepting a T1 transition increases the energy, and so T1 steps are rejected, or because they alternate between T1 events at every timestep. In either case, the geometry and the tensions are such that it is energetically favorable for the edge to remain very short over multiple timesteps, resulting in a "trapped" short edge that functions very much like a multi-fold coordinated vertex. Figure 6(a) shows an integral of these length histogram over all time windows,

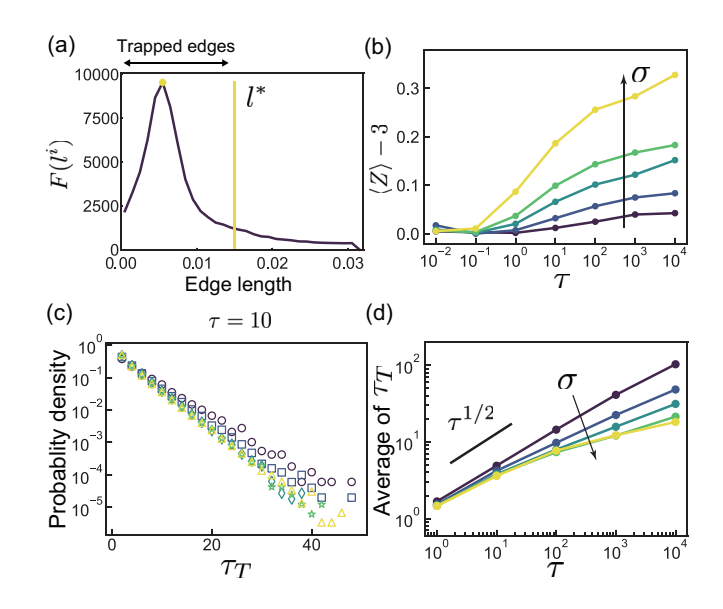


FIG. 6. Properties of the trapped edges. (a) Timeintegrated distribution  $F(l^i)$  is shown. The trapped edges are defined as the population with the peak close to zero edge length by systematically thresholding the edge length by  $l^*$  as indicated by the yellow vertical line. We randomly sampled 100 edges and 200 T1 events for each edge to plot (a). (b) The average vertex coordination number per frame  $\langle Z \rangle$  subtracted by 3 is plotted against  $\tau$ . In (b), we set  $l^* = l_{\text{th}}$  for some data points  $(\tau, \sigma) = (0.01, 0.1/0.15/0.3), (0.1, 0.02)$ , since the distributions  $F(l^i)$  were too broad to determine the threshold  $l^*$  for the trapping edges in these data points. (c) Semi-log plots of the probability distribution of the life time  $\tau_T$  of the trapped edges for  $\tau = 10$ . (d) The average lifetime  $\tau_T$  of the trapped edges is plotted against  $\tau$ . The solid line is a guide for eyes indicating the power law  $\tau^{1/2}$ . In (b-d),  $\sigma \in$ [0.02, 0.05, 0.10, 0.15, 0.30] (from dark color to light color).

 $F(l^i) = \sum_{t_T} f(l^i(t_T))$ , which similarly exhibits a prominent peak  $l \sim 0.05$ , highlighting a characteristic length for edges that are trapped. To formally define "trapped edges", we use this peak to define a new threshold length-scale  $l^*$  shown by the vertical line in Fig. 6(a), that provides an upper bound to the length of the vast majority of trapped edges, see discussion in Appendix A. This allows us to formally define all edges with length  $l < l^*$  as trapped edges that may be functioning as "effective high-order vertices". We can also define a "trapped edge lifetime"  $\tau_T$  corresponding to the number of natural time units where the edge continuously maintains a length less than  $l^*$ .

To quantify the density of these effective higher-order vertices, we calculate  $\langle Z \rangle$ , which is the average vertex coordination number Z=2E/V averaged over the simulation run, where E and V are the number of edges and vertices per timestep [23] and assuming the trapped edges are effectively 4-fold coordinated: if we have no trapped edges and only 3-fold vertices, Z=3. In Fig. 6(b), we plot  $\langle Z \rangle -3$  with respect to  $\tau$  for different  $\sigma$ . We find

that  $\langle Z \rangle - 3$  increases monotonically as  $\tau$  and  $\sigma$  increase.

Moreover, since unlike the system in Ref [23] our system is dynamic, the persistence time of multi-fold coordinated vertices may be important. Therefore, we also investigate the lifetime of trapped edges  $\tau_T$ , with normalized histograms shown in Fig. 6(c) and Supplemental Fig. 9. The distribution is consistent with an exponential in the moderate  $\tau$  regime ( $\tau \sim 10$ ) as shown in Fig. 6(c), while it looks nearly power-law, with a large-scale cutoff, in the large- $\tau$  regime ( $\tau \sim 1000$ , see Supplemental Fig. 9 ). Although the mechanisms driving these distributions remains unclear, we can nevertheless extract the average lifetime of trapped edges  $\langle \tau_T \rangle$  as a function of model parameters, shown in Figure 6(e). The average lifetime of trapped edges increases dramatically with increasing  $\tau$ , and also increases slightly with decreasing  $\sigma$ . Taken together, these results suggest that there is a systematic increase in the fraction and persistence of effectively multi-fold coordinated vertices at large  $\tau$  and  $\sigma$ , which, in the absence of other effects, should tend to rigidify the system.

While a theory for precisely how multi-fold coordinated vertices rigidify a system in the presence of fluctuations does not yet exist, our data provide some clues. First, if we assume there were no additional rigidifiation by multi-fold coordinated vertices, but that in the presence of heterogeneous fluctuations T1 transitions simply take extra time  $\tau_T$  to resolve, we expect the time scale  $1/D \sim \tau_{cr}$  required for cell rearrangements should be  $\tau_{cr} \sim \langle \tau_T \rangle + \tau_l$ , where  $\tau_l$  is the time scale required for an edge to shrink from a typical edge length to zero discussed previously. In the large- $\tau$  regime, data in Fig. 6(d) suggest  $\langle \tau_T \rangle \sim \tau^{\beta}$  with  $\beta \leq 1/2$ . Since in the large- $\tau$  regime  $\tau_l \sim 1/D_l \sim 1/\tau$  is much smaller than  $\tau_T$ , we would predict  $\tau_{cr} \sim \langle \tau_T \rangle \sim \tau^{\beta}$  with  $\beta \leq 1/2$ .

In contrast, in our simulations the plateau in the large- $\tau$  regime in Fig. 5 suggests the large-tau regime scales roughly as  $D \sim \tau^{-1} \sigma^{1/2}$ .

Therefore,  $\tau_{cr}sim\tau$  in our simulations diverges faster than  $\tau^{\beta}$  estimated above by assuming no rigidification via rosette formation. This suggests that the rosette formation, quantified by the density of excess coordinated vertices  $\langle Z \rangle - 3$  that increases dramatically with  $\tau$  (Fig. 6(b)), is directly playing a role in rigidifying the tissue.

One obvious question, especially given the important role of effective multi-fold coordinated vertices, is whether our results depend strongly on our choice of how to resample the stress in the newly created edges after a T1 swap. The "persistent" model we have considered so far gives the new edge after a T1 swap the same tension as the old edge, which will clearly favor trapped edges where the tension is larger and contractile. Therefore, we also investigate more democratic ways of sampling tensions in the new T1 edge, illustrated schematically in Fig 1 (b) and (c), which we term "resetting" and the "resampling" models.

Figure 7(a) shows that, as expected, resetting and re-

sampling models generate the same diffusion constants as the persistent models in the low- $\tau$  regimes, consistent with the hypothesis that fluctuation-driven diffusion, which should be the same in all models, dominates at low  $\tau$ . In addition, there is still non-monotonic behavior in all three models, with the diffusion constant decreasing at large  $\tau$ . However, there is an obvious increase in the diffusion constant at larger  $\tau$  in the resetting and resampling models compared to the persistent model, suggesting that there are fewer effective multi-fold coordinated vertices in the model where the edge tension changes after the swap. This is confirmed in Fig. 7(b), which shows that the fraction of multi-fold coordinated vertices is indeed lower for resetting or resampling models compared to the persistent model, although the effect still persists.

#### III. DISCUSSION

Taken together, these results suggest that in tissues with fluctuating tensions, there will always be a competition between fluidification due to active fluctuations and rigidification due to the formation of effectively multi-fold coordinated vertices. In general, increasing the magnitude of the tension always increases the fluidity of the tissue, while increasing the persistence of fluctuations has a non-monotonic impact on tissue fluidity. For short persistence times, the diffusivity is dominated by fluctuations and increases with increasing persistence. We confirm this by predicting and demonstrating a scaling collapse of our data in this regime.

In contrast, for larger persistence times the cell dynamics are dominated by the rigidification causes by effectively multi-fold coordinated vertices. The precise details of the balance and the crossover persistence timescale depend on how tensions form on new cell-cell interfaces after a cellular rearrangement, which we demonstrate by analyzing several different models for this process.

Our results are entirely consistent with independent work recently published by Kranjc [19], which focused only on the small- $\tau$  regime and found a simple monotonic relationship between  $\sigma$ ,  $\tau$ , and the diffusivity.

However, it is reasonable to expect that fluctuations in stress, generated by correlated and cooperative localization of large number of cytoskeletal molecules, may persist longer than the natural time unit in these simulations, which roughly corresponds to the time required for cells to find a new stable state after executing a T1 transition. For example, rough estimates for rearrangement timescales from experiments in Drosophila are typically less than 10 minutes [34], while fluctuations in tensions due to mechanisms like planar cell polarity can last upwards of 30 minutes [34], and multi-fold coordinated vertices are often observed in such systems. Therefore, the large- $\tau$  regime dominated by effectively multi-fold coordinated vertices, explored here for the first time, is likely to be relevant for many experiments.

One important point is that in this dynamic simulation, we had to develop a systematic and robust method for identifying vertices that were effectively multi-fold coordinated. In our simulations, such vertices actually consist of 3-fold coordinated vertices joined by one or more very short edges, which are trapped in that configuration by the dynamics. We note that similar methods exist in experiments; microscopy resolution limits a researchers' ability to distinguish truly 4-fold coordinated vertices from very short edges and in practice all edges less than a threshold (typically 10% of a typical edge length) are lumped in with multi-fold coordinated vertices [17]. By identifying Effective multi-fold coordinated vertices in this way, we were able to make a connection with the work in static systems showing rosettes induce rigidification [23].

Nevertheless, many open questions remain. Strictly speaking, the constraint counting argument developed in [23] depends on the fact that multi-fold coordinated vertices explicitly reduce the number of degrees of freedom available to the system. This is not the case for our effective multi-fold coordinated vertices, where the total number of degrees of freedom remains constant. On the other hand, very short, high tension edges do place strong constraints on the dynamics of the attached vertices. As shown by some of us in ref. [33], such short edges in systems with heterogeneous tensions can generate cusps in the potential energy landscape that can trap vertices. Therefore, future work could focus on using some of these idea to generalize the static arguments made in [23] to explain enhanced rigidity in dynamic systems. In particular, it would be interesting to know what sets the characteristic lengthscale for trapped edges, and whether it depends on an effective temperature driving fluctuations.

From an experimental perspective, our work clarifies that fluctuating tensions can drive either fluidization or rigidity depending on the parameter regime. Given that the tension dynamics just after T1 transitions play an important role in this balancing act, it would be especially useful to gather data, using tools such as laser ablation or optogenetics, about how these tensions evolve in different in vivo and in vitro systems. As the rigidity/fludity of biological tissues can help set timescales for processes like body axis elongation [15, 17] or wound healing, it could be that organisms tune the magnitude or persistence time of stress fluctuations to control such processes. It would be interesting to look for such trends in model organisms.

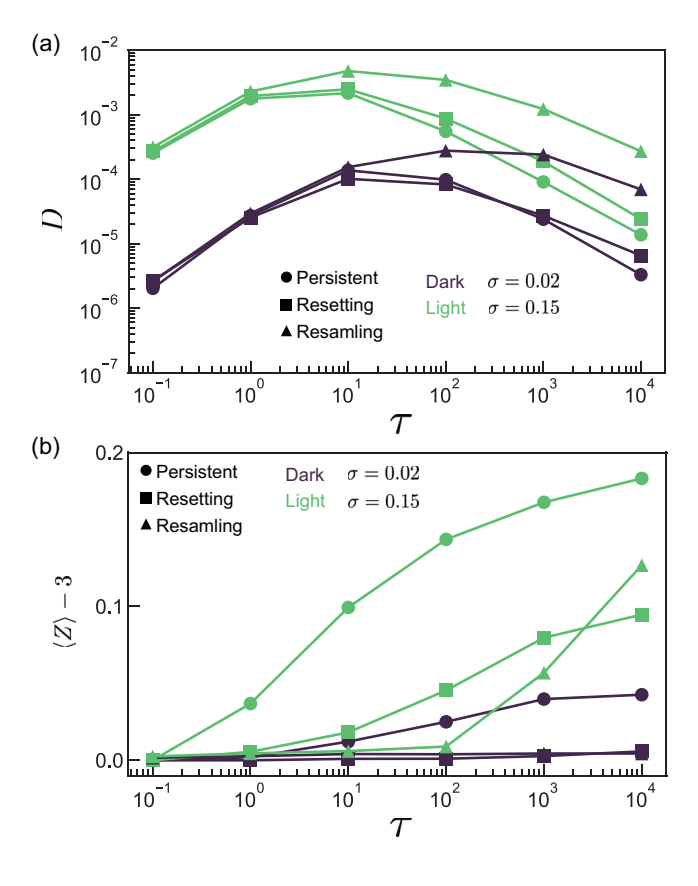


FIG. 7. Comparison of D and  $\langle Z \rangle - 3$  among three models: the persistent model (circle), the resetting model (square), the resampling model (triangle). (a)(b) D and  $\langle Z \rangle - 3$  are plotted against  $\tau$  for three models, respectively. Purple and green markers represent the data with  $\sigma = 0.02$  and  $\sigma = 0.15$ , respectively. The distributions  $F(l^i)$  were too broad to determine the threshold  $l^*$  for the trapping edges in the following data points:  $(\tau,\sigma)=(0.1,0.02)$  in the persistent model,  $(\tau,\sigma)=(0.1,0.02/0.15),(1,0.02)$  in the resetting model,  $(\tau,\sigma)=(0.1,0.02/0.15),(1,0.02/0.15),(10,0.02/0.15),(100,0.02),(1000,0.02),(10000,0.02)$  in the resampling model. We hence set  $l^*=l_{\rm th}$  for these data points.

# CONFLICTS OF INTEREST

There are no conflicts to declare.

# ACKNOWLEDGMENTS

This work is supported by Grant-in-Aid for JSPS Fellows (Grant No. 18J01239), KAKENHI Grant No. 17H07366 and RIKEN HOKUSAI supercomputer systems (Project Q19433) to T.Y.

# Appendix A: Definition of the threshold $l^*$ of the trapped edges

We first detected a maximum peak at  $l=l_{\rm max}$  in the time-integrated distribution  $F(l^i)$  as indicated by a yellow circle marker in Fig. 6(a). We next subtracted the minimum frequency in the range  $l_{\rm max} \leq l \leq l_{\rm th}$ , as the background, from the time-integrated distribution. Using this background-subtracted distribution, we finally determined the threshold  $l^*$  as the minimum edge length at which the frequency is below 10% of the maximum frequency at  $l=l_{\rm max}$ .

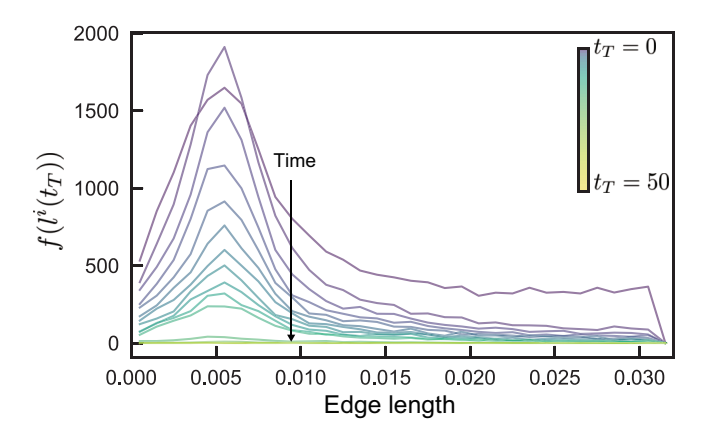


FIG. 8. The time-evolution of the distribution  $f(l^i(t_T))$  of the length  $l^i(t_T)$  of the edges experiencing T1 events. The data for  $\tau=10$  and  $\sigma=0.15$  is shown as an example. The color of the curves logarithmically maps the time  $t_T$  ranging between 0 and 50 natural time unit.

Appendix B: Probability distribution of life time  $\tau_T$  of trapped edges

In Fig. 9, we show the semi-log and log-log plots of the probability distribution of the life time  $\tau_T$  of the trapped edges for  $\tau = 1000$ .

- T. Ariga, M. Tomishige, and D. Mizuno, Phys. Rev. Lett. 121, 218101 (2018).
- [2] T. Ariga, M. Tomishige, and D. Mizuno, Biophys Rev 12, 503 (2020).
- [3] K. Hayashi, Biophys Rev 10, 1311 (2018).
- [4] T. Yanagida, M. Iwaki, and Y. Ishii, Phil. Trans. R. Soc. B 363, 2123 (2008).
- [5] S. Toyabe, T. Watanabe-Nakayama, T. Okamoto, S. Kudo, and E. Muneyuki, Proceedings of the National Academy of Sciences 108, 17951 (2011).
- [6] D. A. Fletcher and R. D. Mullins, Nature 463, 485 (2010).
- [7] K. M. Yamada and M. Sixt, Nat Rev Mol Cell Biol 20, 738 (2019).
- [8] A. M. Klein and B. D. Simons, Development 138, 3103 (2011).
- [9] M. J. F. Barresi and S. F. Gilbert, Developmental Biology, 12th ed. (2019).
- [10] T. Mammoto and D. E. Ingber, Development 137, 1407 (2010).
- [11] J. H. Shawky and L. A. Davidson, Developmental Biology 401, 152 (2015).
- [12] N. I. Petridou and C.-P. Heisenberg, EMBO J 38 (2019).

- [13] J.-A. Park, J. H. Kim, D. Bi, J. A. Mitchel, N. T. Qazvini, K. Tantisira, C. Y. Park, M. McGill, S.-H. Kim, B. Gweon, J. Notbohm, R. Steward Jr, S. Burger, S. H. Randell, A. T. Kho, D. T. Tambe, C. Hardin, S. A. Shore, E. Israel, D. A. Weitz, D. J. Tschumperlin, E. P. Henske, S. T. Weiss, M. L. Manning, J. P. Butler, J. M. Drazen, and J. J. Fredberg, Nature Materials 14, 1040 (2015).
- [14] É. Fodor, V. Mehandia, J. Comelles, R. Thiagarajan, N. S. Gov, P. Visco, F. van Wijland, and D. Riveline, Biophysical Journal 114, 939 (2018).
- [15] A. Mongera, P. Rowghanian, H. J. Gustafson, E. Shelton, D. A. Kealhofer, E. K. Carn, F. Serwane, A. A. Lucio, J. Giammona, and O. Campàs, Nature 561, 401 (2018).
- [16] T. E. Angelini, E. Hannezo, X. Trepat, M. Marquez, J. J. Fredberg, and D. A. Weitz, Proceedings of the National Academy of Sciences 108, 4714 (2011).
- [17] X. Wang, M. Merkel, L. B. Sutter, G. Erdemci-Tandogan, M. L. Manning, and K. E. Kasza, Proc Natl Acad Sci USA 117, 13541 (2020).
- [18] D. M. Sussman, M. Paoluzzi, M. Cristina Marchetti, and M. Lisa Manning, EPL (Europhysics Letters) 121, 36001 (2018).
- [19] M. Krajnc, Soft Matter (2020).

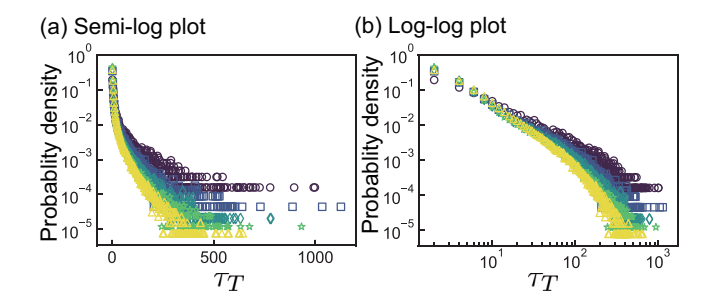


FIG. 9. The probability distribution of the life time  $\tau_T$  of the trapped edges. (a) Semi-log and (b) log-log plots of the probability distribution  $\tau_T$  for  $\tau=1000$ .  $\sigma\in[0.02,0.05,0.10,0.15,0.30]$  increase from dark color to light color (circle: $\sigma=0.02$ , square: $\sigma=0.05$ , diamond: $\sigma=0.10$ , star: $\sigma=0.15$ , triangle: $\sigma=0.30$ ).

- [20] S. Kim, M. Pochitaloff, Georgina-Stooke-Vaughan, and O. Campàs, Embryonic Tissues as Active Foams, Preprint (Biophysics, 2020).
- [21] D. Bi, X. Yang, M. C. Marchetti, and M. L. Manning, Physical Review X 6 (2016).
- [22] M. Chiang and D. Marenduzzo, EPL 116, 28009 (2016).
- [23] L. Yan and D. Bi, Phys. Rev. X 9, 011029 (2019).

- [24] M. J. Harding, H. F. McGraw, and A. Nechiporuk, Development 141, 2549 (2014).
- [25] G. Trichas, A. M. Smith, N. White, V. Wilkins, T. Watanabe, A. Moore, B. Joyce, J. Sugnaseelan, T. A. Rodriguez, D. Kay, R. E. Baker, P. K. Maini, and S. Srinivas, PLOS Biology 10, e1001256 (2012).
- [26] J. T. Blankenship, S. T. Backovic, J. S. P. Sanny, O. Weitz, and J. A. Zallen, Developmental Cell 11, 459 (2006).
- [27] A. Das, S. Sastry, and D. Bi, arXiv:2003.01042 [cond-mat, q-bio] (2020), arXiv:2003.01042 [cond-mat, q-bio].
- [28] S. Curran, C. Strandkvist, J. Bathmann, M. de Gennes, A. Kabla, G. Salbreux, and B. Baum, Developmental Cell (2017).
- [29] H. Honda, H. Yamanaka, and M. Dan-Sohkawa, Journal of Theoretical Biology 106, 423 (1984).
- [30] D. Bi, J. H. Lopez, J. M. Schwarz, and M. L. Manning, Nature Physics 11, 1074 (2015).
- [31] A. S. Bodrova, A. V. Chechkin, A. G. Cherstvy, H. Saf-dari, I. M. Sokolov, and R. Metzler, Sci Rep 6, 30520 (2016).
- [32] M. A. Spencer, Z. Jabeen, and D. K. Lubensky, The European Physical Journal E 40 (2017).
- [33] D. M. Sussman, J. M. Schwarz, M. C. Marchetti, and M. L. Manning, Phys. Rev. Lett. 120, 058001 (2018).
- [34] K. E. Kasza, D. L. Farrell, and J. A. Zallen, Proceedings of the National Academy of Sciences 111, 11732 (2014).